

Long-range order Bragg scattering and its effect on the dynamic response of a Penrose-like phononic crystal plate

Domenico Tallarico^{✉,*}, Andrea Bergamini[✉], and Bart Van Damme[✉]

EMPA, Laboratory for Acoustics/Noise Control, Überlandstrasse 129, 8600 Dübendorf, Switzerland



(Received 29 August 2022; revised 24 March 2023; accepted 21 April 2023; published 4 May 2023)

In this article, we present scattering and localization phenomena in a thin elastic plate comprising an aperiodic arrangement of scatterers. By analyzing the form factor of the scattering cluster, we sample the reciprocal space which shows strong scattering points in reciprocal space associated with nontrivial dynamic response. Specifically, we identify attenuating frequency regimes and bands where strong localization is predicted and experimentally observed. We show that both localization and attenuation are Bragg scattering phenomena, induced by the long-range aperiodic patterns. Illustrative comparisons are drawn with a periodic counterpart having the same density of scatterers. The novel findings are corroborated by analytical estimates, numerical finite-element predictions, and vibrometric experiments. The results are relevant for the research community interested in extending phononic crystal phenomena to lower frequencies.

DOI: [10.1103/PhysRevB.107.174201](https://doi.org/10.1103/PhysRevB.107.174201)

I. INTRODUCTION

Quasicrystals are ordered tessellations of space without translational symmetry. The first natural quasicrystal featuring icosahedral point-group symmetry—inconsistent with lattice translations—was reported in the early 1980s by Shechtman *et al.* [1]. At the same time, solid-state physics have inspired theoretical and experimental studies into metamaterials, man-made structures whose exceptional dispersive properties have found applications into many branches of classical physics, such as photonics, acoustics, continuum mechanics, and thermodynamics, providing solutions to plenty of engineering problems. At the basis of metamaterials' pervasive success, there is the so-called Bloch-Floquet theorem which guarantees that the fundamental solutions of periodically modulated structures can be traced back to the solution of relatively cheap eigenvalue problems. Microstructured periodic thin plates (also referred to as platonic crystals [2]) are an active research area due to the importance of slender bodies to noise emission. Several microstructures have been investigated: among those analytically treatable, we mention perforated thin plates [3–5], arrays of pinned pointwise constraints [6], arrays of unsprung [7], and sprung point masses [8,9] with and without defects.

Locally resonant metamaterials are particularly suitable for structural dynamics applications due to the fact that their constituents are active in the deep subwavelength regime. The resonating scatterers are placed less than half a wavelength apart, resulting in a high imaginary part of the wave number and, thus, rapidly decaying elastic waves. However, such sub-wavelength behavior is accompanied by narrow-band effects. On the other hand, the frequency bands for dispersive effects in phononic crystals are inherently linked to the size of the unit

cell (UC), whereas being wider compared to locally resonant counterparts.

Limited attention has been given so far to aperiodic phononic quasicrystals. One-dimensional examples have been reported with a focus on longitudinal elastic wave dynamics in Fibonacci-like rods [10]; flexural wave dynamics in beams with their thickness modulated according to incommensurable periodicities [11]; topological band gaps in beams with aperiodically modulated local resonances [12]. In two dimensions, Beli *et al.* [13] introduced by-design decoration of plates featuring pointwise Bragg peaks with eightfold, tenfold, and 14-fold rotational symmetry. The authors also report highly isotropic wave propagation within the aperiodic composites. The results are extended in Ref. [14] to account for wave beaming.

In the present article, we give attention to the effect of long-range order in a P3 Penrose quasicrystal [15] on the dynamic response of finite clusters of resonators (either embedded into an infinite plate or hosted by a finite plate). Such a quasicrystal can be constructed by a so-called *deflation/inflation* tiling, illustrated in Fig. 1. We give a concise introduction, and we refer to Ref. [16] for a more detailed discussion. Each rhombus [panel (a)] can be divided into two isosceles triangles. Each pair of triangles [A, A' and B, B' , see Fig. 1(b)] differ by the way equal sides are decorated (either a circle or a square appear on the right-hand side of the top vertex). Rhombi are obtained by joining the pair elements along the “starred” side. Adjacent rhombuses are added by joining triangles along equal sides, i.e., sharing the same length and symbol, a process referred to as *inflation*. Each triangle is decomposed according to the rules outlined in Fig. 1(c) where we show only the first level of decomposition. An arbitrary level of decomposition can be obtained by applying the rules to the inner triangles, giving rise to a so-called *deflation* rule. In this paper, we decompose the BB' rhombus [Fig. 1(a)]. The n th level of decomposition induces the rhombuses' length side

*domenico.tallarico@gmail.com

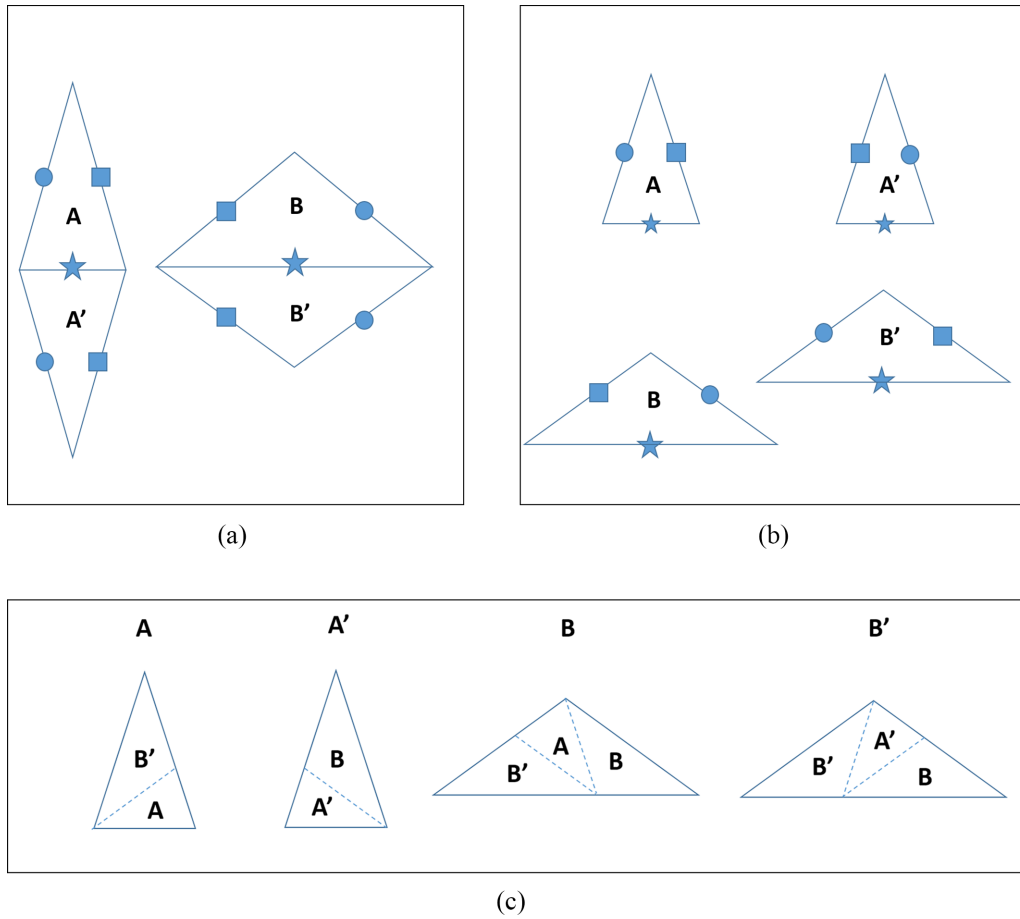


FIG. 1. Panel (a) shows the thick and thin rhombuses, each of which comprise the triangle pair A, A' and B, B' [see panel (b)]. Owing to the decoration of their sides, the triangles within each pair transform into one another via reflection about their height [see panel (b)]. Panel (c) shows the first decomposition rule for each of the four triangles in panel (b). Iterating the decomposition on the initial sets of triangles leads to the P3 Penrose tessellation.

$\ell_n = [2 \sin(\vartheta_0)]^{-n} \ell_0$ with $\vartheta_0 = 54^\circ$. A Matlab implementation [17] of the tessellation has been used to generate the aperiodic distribution of scatterers.

We note that aperiodic tilings of the plane can also be introduced via *cut-and-project* [18], i.e., by projecting part of the four-dimensional periodic tiling onto a two-dimensional subspace. Since the number of possible symmetries increases with dimensions, the projected aperiodic counterparts inherit possible underlying fivefold, eightfold, tenfold, or 12-fold symmetry. Formal results exist showing the pointwise nature of the n -fold diffraction pattern of several cut-and-project lattices. Although establishing such formal results for inflation/deflation structures is notoriously more complicated (see Ref. [16] for a recent discussion), assuming that the scattering potential is a Dirac comb leads to a closed-form expression for the structure factor and allows the identification of Bragg peaks [see Sec. (II C)]. The main focus of the present article is to single out the effect of Bragg scattering of flexural waves in a thin plate due to the presence of a P3 Penrose cluster of mass scatterers. After fixing the decomposition level, we associate an elastic stud to the center of mass of each resulting triangle (of type A, A', B or B'). Endowing rigid scatterers with rotational degrees of freedom and the corresponding inertia, allows a realistic representation

of the experimental setup, adding complexity to the case of point-mass scatterers as described in Sec. III. In this article, we focus on the distribution of scatterers represented in Fig. 2.

The number of scatterers at the i th decomposition levels can be evaluated by accounting for the total number of A and A' triangles (N_A), and the total number of B and B' triangles (N_B). Specifically, from Fig. 1(c), the following recursive relations for the total number of triangles can be inferred

$$\begin{aligned} N_A^{(i)} &= N_A^{(i-1)} + N_B^{(i-1)}, \\ N_B^{(i)} &= N_A^{(i-1)} + 2N_B^{(i-1)}, \quad i = 1, \dots, n, \end{aligned} \quad (1)$$

which allows to calculate $N_A = N_A^{(n)}$ and $N_B = N_B^{(n)}$, and, therefore, $N_s = N_A + N_B$, given a seed number of initial triangles $N_A^{(1)}$ and $N_B^{(1)}$.

The article is organized as follows. In Sec. II, we present the Penrose-like distribution of scatterers as well as the governing equations, useful to describe the phononic crystal under consideration. In Sec. III, we present and discuss the results concerning both a finite cluster of nonresonant scatterers hosted by an infinite plate and a finite plate hosting the same arrangement of scatterers. Finally, in Sec. IV, we summarize the results and give our main conclusions.

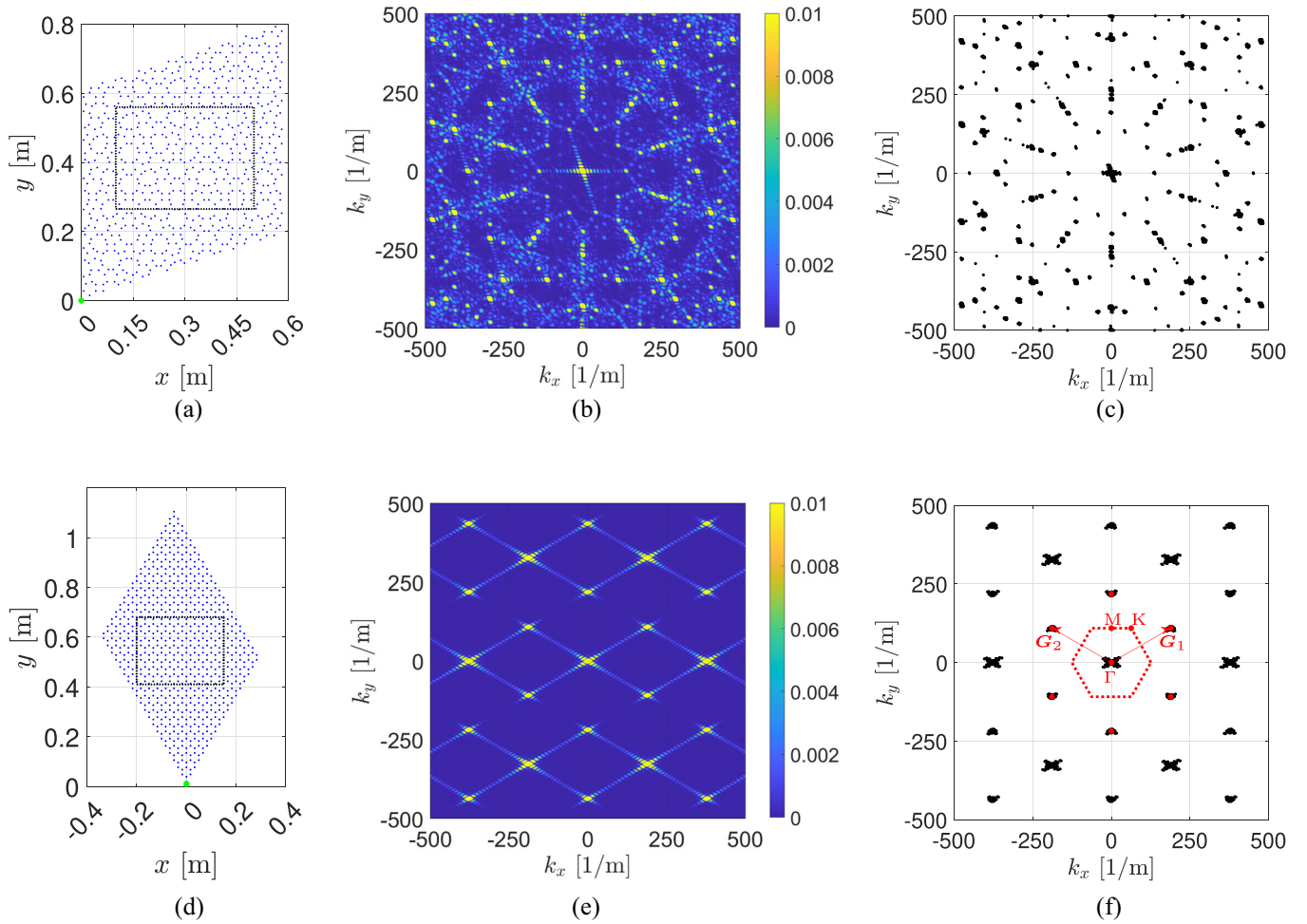


FIG. 2. (a) Distribution of Penrose-like scatterers obtained by decomposing $n = 6$ times a thick rhombus with side length $L_0 = 0.617$ m. (b) Fourier transform of the structure factor [Eq. (5)] corresponding to the distribution of scatterers in panel (a). (c) A set of local maxima in panel (b) corresponding to Bragg peaks in reciprocal space of the P3 lattice. The maxima are obtained by selecting wave vectors (black dots) for which the structure factor exceeds the threshold $\alpha = 0.01$. (d) Equivalent honeycomb cluster of scatterers. Panels (e) and (f) have been obtained similar to panel (b) and (c) for the arrangement in panel (d). In panel (f), the red dotted hexagon represents the boundaries of the first Brillouin zone (BZ) of the triangular lattice, whereas the red arrows mark the primitive vectors in reciprocal space. The high-symmetry points Γ , M , and K , as well as the nearest-to- Γ neighbor nodal points are marked by red circles. The areas enclosed by the dashed rectangles in panels (a) and (d) represent probing regions of the structured plates.

II. STRUCTURES AND ASSOCIATED GOVERNING EQUATIONS

A. Flexural waves in thin elastic plates

Time-harmonic flexural waves in a thin plate comprising a cluster of resonators are governed by the partial differential equation [7–9],

$$\mathcal{L}\psi(\mathbf{r}) = f(\beta) \sum_{j=1}^{N_s} \delta(\mathbf{r} - \mathbf{r}_j) \psi(\mathbf{r}), \quad (2)$$

where $\psi(\mathbf{r})$ is the time-harmonic flexural field at the spatial coordinate \mathbf{r} on the plane, and \mathbf{r}_j , $j = \{1, \dots, N_s\}$, is the coordinate's vector of the j th-scatterer with N_s being the number of scatterers. In Eq. (2), we introduce the operator $\mathcal{L} = \Delta^2 - \beta^4$ with Δ^2 as the biharmonic operator and

$$\beta(\omega) = \left(\frac{\rho_s h \omega^2}{D} \right)^{1/4}, \quad (3)$$

as the wave number, where ω is the angular frequency, ρ_s is the mass density and $D = E_s h^3 / [12(1 - \nu_s^2)]$ is the flexural rigidity with h , E_s , and ν_s being the thickness, Young's modulus, and Poisson's ratio, respectively. The subscript “s” denotes steel, namely, $\rho_s = 7850$ kg/m³, $E_s = 200$ GPa, and $\nu_s = 0.3$.

The Green's function associated with the operator \mathcal{L} [i.e., the solution of $\mathcal{L}g_0(\mathbf{r}, \mathbf{r}') = \delta(\mathbf{r} - \mathbf{r}')$] is [19]

$$g_0(\mathbf{r}, \mathbf{r}'; \beta) = \frac{i}{8\beta^2} \left(H_0^{(1)}(\beta|\mathbf{r} - \mathbf{r}'|) + \frac{2i}{\pi} K_0(\beta|\mathbf{r} - \mathbf{r}'|) \right), \quad (4)$$

where $H_0^{(1)}(\beta|\mathbf{r}|)$ and $K_0(\beta|\mathbf{r}|)$ are the Hankel function of the first kind and the modified Bessel function of the second kind, respectively. The solution of the scattering problem to an incident field can be obtained by using the Korringa-Kohn-Rostoker [20,21] (KKR) also known as the multiple-scattering method [22], which builds upon the knowledge of the Green's

function of the homogeneous operator and the scattering potential $f(\beta)$ in the right-hand side of Eq. (2). Details of the derivation are provided in Appendix A. We observe that $f(\beta)$ can be any function of frequency resulting from the physics of the considered scatterers. However, it should be pointed out that the model in Eq. (2) is accurate only for scatterers exerting purely normal forces with respect to the plate and vanishing moments. In general, the finite extent of passive scatterers, their nonzero rotational inertia and their possible asymmetry about the neutral plane of the plate, provide a coupling route between the rotation and in-plane fields of the plate. This calls for the need to consider a system of plane-stress in-plane PDEs coupled with the flexural field by the boundary conditions between the plate and the scatterers. The study of a more general class of problems dealing with plate-affixed Euler-Bernoulli beams [23] has revealed that the solution based on the Green's function is of the singularly perturbed type. We expect to encounter a similar kind of singular behavior for the special case of scatterers (rigid studs) investigated in the present paper (see Sec. III), this solution route being, therefore, beyond scope. We refer to Ref. [24] for a detailed treatment of the solution regularization for the plate's plane-stress/flexural field problem within plates, coupled by Euler-Bernoulli beams' junctions.

B. Distribution of scatterers

By using the recurrence relation (1) with seeds $N_A^{(0)} = 0$ and $N_B^{(0)} = 2$, it is possible to verify that the total number of scatterers associated with the decomposition level $n = 6$ is $N_s = 754$ [25]. The resulting spatial distribution of scatterers in the truncated P3 Penrose lattice is represented in Fig. 1(a) by the blue dots.

The average scatterers' density N_s/S with S being the surface of the plate can be used to define a periodic counterpart of the proposed aperiodic plate. For illustrative purposes, we opt for a honeycomb lattice because of the two scatterers per UC pattern reminiscent of our P3 Penrose arrangement. In addition, the underlying triangular lattice features isotropic low-frequency dispersion compared to other Bravais lattices in two dimensions [26]. The resulting graphenelike structure has been analyzed by Torrent *et al.* [9] with a focus on the emergence of Dirac-like dispersion and associated dynamic response of waveguides.

In order to provide a meaningful comparison, especially in view of the finite plate response, we aim at preserving the total mass of the studded plate as well as the average density of scatterers. Approximately, the same number of scatterers is given by the choice $N_1, N_2 \approx N_s/2$, where $N_1, N_2 \in \mathbb{N}$ represent the number of unit cells along the directions identified by the primitive vectors of the triangular lattice. Therefore, we guarantee the same total mass by requiring that the triangular lattice primitive vectors have magnitude $\bar{\ell} = [2S/(\sqrt{3}N_1N_2)]^{1/2}$. Focusing on the specific case represented in Fig. 2, $N_1 = 18$ and $N_2 = 21$ represent a suitable choice, corresponding to primitive lattice vectors' magnitude $\bar{\ell} = 0.033$ m. By choosing the primitive vectors to be $\mathbf{t}_j = \bar{\ell}/2[(-1)^{j-1}, \sqrt{3}]^T$ with $j = 1, 2$, the reciprocal lattice vectors are $\mathbf{G}_j = 2\pi/(\bar{\ell}\sqrt{3})[\sqrt{3}(-1)^{j-1}, 1]^T$.

C. Structure factor and diffraction patterns

In reciprocal space, the structure factor is defined as the modulus squared of the Fourier transform of the scattering potential [see the right-hand side of Eq. (2)], normalized by the amplitude $f(\beta)$, i.e.,

$$\mathcal{F}(\mathbf{k}) = \left| \frac{1}{N_s} \sum_{j=1}^{N_s} \exp(i\mathbf{k} \cdot \mathbf{r}_j) \right|^2, \quad (5)$$

where the index $j = 1, \dots, N_s$ runs over the Penrose distribution of scatterers at the coordinates \mathbf{r}_j on the plane, and $\mathbf{k} = (k_x, k_y)^T$, is the wave vector. The quantity is customarily used in condensed-matter physics to analyze particle or wave diffraction experiments as it is proportional to the scattering cross section. As the name suggests, the structure factor contains important crystallographic information on the atomic distribution. It quantifies the diffraction intensity in reciprocal space, thus, allowing an approximate identification of the Bragg peaks, induced by a finite but large distribution of scatterers. Bragg peaks are special wave vectors at which strong dispersive behavior, such as the opening of band gaps, is expected. The evaluation of structure factors is customarily used in the research community interested in aperiodic media [27].

Figure 2(b) shows the Fourier transform of the structure factor for the Penrose cluster, evaluated using Eq. (5) with scatterer's coordinates as per Fig. 2(a). The figure shows bright pointwise spots, approximately identifying the Bragg peaks associated with our Penrose lattice. This is made more evident by showing only those wave numbers at which the structure factor exceeds a given threshold [Fig. 2(a)]. It is visually evident that the first two rings show a tenfold symmetric pattern. A similar analysis conducted on the periodic counterpart in Fig. 2(d) reveals the Bragg peaks for the triangular lattice with the classic sixfold symmetric pattern [see Figs. 2(e) and 2(f)], in good agreement with the corresponding primitive vectors (cf. Sec. II B).

D. Heuristic low-frequency dispersive properties

At low frequency, the effect of the scatterers can be accounted for by introducing an effective material density,

$$\rho = \rho_s + \frac{mN_s}{Sh}, \quad (6)$$

where m is the mass of each scatterer and S is the surface of the enclosing plate. The low-frequency dispersion for flexural waves in the long-wavelength regime can be easily obtained by evaluating the dispersion relation in Eq. (3), using Eq. (6) as mass density, i.e.,

$$\omega^* \approx \sqrt{\frac{D}{\rho h}} |\kappa|^2, \quad (7)$$

where the density ρ has been introduced in Eq. (6), and $\kappa = (\kappa_x, \kappa_y)^T$ being the Bloch wave vector. A heuristic argument that justifies Eq. (7) is provided as follows. As the frequency of the impinging wave decreases, the corresponding wavelength comprises more and more point masses. Since the plate is not stiffened by the presence of the point scatterers,

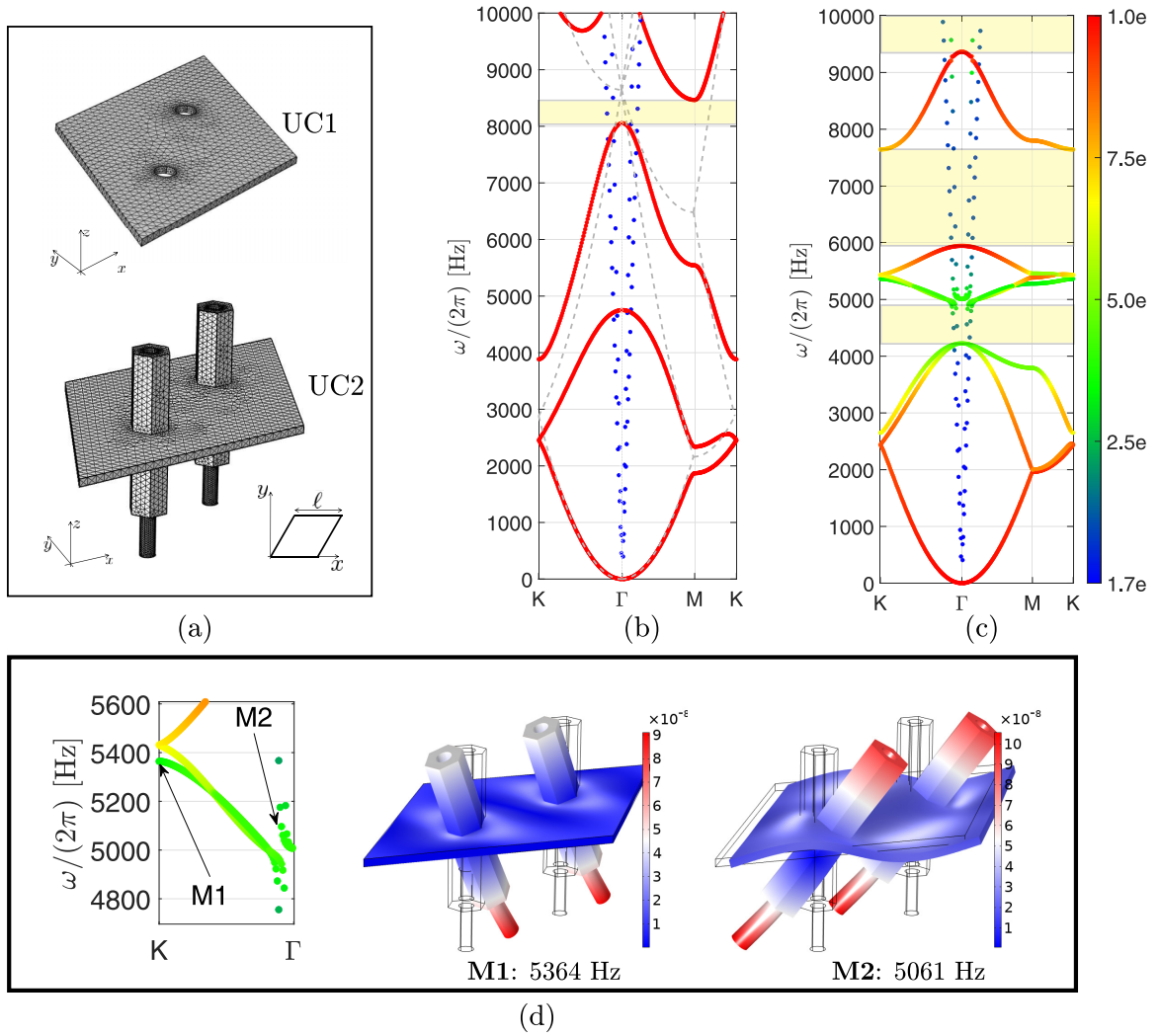


FIG. 3. (a): Two honeycomb unit-cells (UC1 and UC2). UC1 consists of two drilled holes with mass m homogeneously distributed along their edge, whereas in UC2 the holes host two rigid studs of mass m (see the inset). The radius of the holes is $r = 1.5$ mm, and the mass of the scatterers is $m = 3.2$ g. Panels (b) and (c) show the dispersion diagrams of UC1 and UC2, respectively, projected over the irreducible BZ (IBZ) in Fig. 4(a). The color represents the degree of polarization of the corresponding mode $p = \int_{UC} |u_z|/|\mathbf{u}| d^3\mathbf{r}$ with blue and red referring to purely in-plane and purely flexural polarization, respectively. The gray dashed lines in panel (b) represent the dispersion of a homogeneous plate with density as in Eq. (6), folded in the first IBZ of the triangular lattice. Panel (d) shows (on the left) a magnification of panel (c) where the arrows mark coordinates of two selected Bloch-Floquet eigenmodes, $M1$ and $M2$ (two rightmost figures). The color legend maps the modulus of the displacement (magnified by a factor 10^5 to appreciate the deformation).

the only property affected by the presence of the scatterers is an overall increase in the density as stated in Eq. (6). As shown in Sec. III A, Eq. (7) is equivalent to the low-frequency dispersive behavior of the periodic counterparts. We refer to Ref. [7] for more formal asymptotic arguments leading to the expression (6).

III. RESULTS AND DISCUSSION

A. Effect of the scatterers finite size on the dispersion of periodic counterparts

In order to single out the scatterers' finite-size effects, we opt to analyze the dispersive properties of the honeycomb UC with different modeling assumptions, as detailed in Appendix B. The focus is on the dispersive properties of two unit cells for a honeycomb lattice UC1 and UC2 in Fig. 3(a).

In UC1, we consider an edge distribution of mass (3.25 g in total) along the circumference of each hole with radius 1.5 mm. In UC2, the scatterers are modeled explicitly and pierce the plate through the same holes as in UC1. The studs are made out of brass (density $\rho_b = 10610$ kg/m³, Young's modulus $E_b = 97$ GPa, and Poisson's ratio $\nu_b = 0.3$). The precise geometry can be accessed on the website of the manufacturer [28]. In Table I, we report the key physical parameters of the studs, relevant to their rigid formulation, namely, the mass (m), the moments of inertia around the x -, y - (I_x and I_y , respectively), and the vertical offset of the center of mass from the midsurface of the plate (h_z). This latter parameter models the fact that the stud is not symmetric about the midplane of the plate. The UC length ℓ has been derived from the considerations in Sec. II C.

TABLE I. Physical parameters of the rigid studs and of the homogeneous plate.

Stud				Plate			
m (g)	I_x (kg m ²)	I_y (kg m ²)	h_z (mm)	E_s (GPa)	ν_s [–]	ρ (kg/m ³)	h (mm)
3.25	1.50×10^{-7}	1.50×10^{-7}	–1.07	200	0.3	7850	1.01

The dispersion diagrams considered in this section have been calculated using the indirect Bloch-Floquet method (readily available in COMSOL MULTIPHYSICS) and a three-dimensional (3D) elasticity formulation without rigid-body assumptions for the studs (see Appendix B for further details). Results are presented along the border of the irreducible Brillouin zone $[\Gamma MK \Gamma]$ in Fig. 2(f). Figure 3(b) shows that, in the long-wavelength regime (i.e., below 1000 Hz) the dispersion diagram is well captured by that of a homogeneous plate with density as in Eq. (6), which have been folded onto the boundaries of the IBZ (see the gray dashed lines) for ease of comparison. Unsurprisingly, as the frequency increases, marked departures from the homogeneous dispersive behavior [see Eq. (7)] arise in both Figs. 3(b) and 3(c). Nevertheless, the gray dashed curve in Fig. 3(b) shows that Eq. (7) is still useful in predicting the approximate band-gap frequency.

Accounting for the finite extent of the studs and their asymmetry with respect to the plate neutral plane leads to fundamentally different features. First, the dispersion of UC1 does not feature any coupling between in-plane and flexural waves. The absence of coupling emerges from the purely flexural and purely in-plane polarization, i.e., by the blue and red color, respectively, in Fig. 3(b). On the other hand, the dispersive properties of the UC2 feature hybridization of in-plane and flexural dispersion branches around 4000 Hz, a phenomenon stemming from two causes: (i) the activation of the rotational inertia and (ii) the asymmetry of the studs with respect to the midplane. We illustrate such hybridization in Figs. 3(d) and 3(e) where we reproduce selected eigenmodes close to the high-symmetry points K and Γ , respectively [cf. Fig. 3(c) for the corresponding Bloch wave vector].

UC1 features a single Bragg-scattering band gap at ≈ 8000 Hz as highlighted by the yellow-shaded rectangle in Fig. 3(b). By contrast, Fig. 3(c) shows more pronounced filtering properties for flexural waves (see the width of the yellow-shaded rectangles). The higher band gap in frequency is clearly controlled by the mass of the scatterers, whereas the lower one is controlled by the rotational inertia coupling with the plate rotation field [i.e., with the derivatives of the flexural field $\psi(\mathbf{r})$].

B. Bragg scattering by phononic clusters within an infinite thin plate

In this section, we study the dynamic response of the clusters of scatterers represented in Figs. 2(a) and 2(d). By solving Eq. (2) with the method outlined in Appendix A, it is possible to probe a finite cluster of point masses in a infinite thin plate, illuminated with an external incident field. We deliberately focus on a cluster made of point masses without resonant effects for which [7–9]

$$f_i(\beta) = \frac{m}{\rho h} \beta^4, \quad \forall i = \{1, \dots, N_s\}, \quad (8)$$

in Eq. (2) with m being the mass of the scatterers. For simplicity, we assume that the incident field originates from a point source generated by a unit force, although other solutions compatible with the Kirchhoff plate can be chosen, e.g., incident plane waves. The cluster, arranged as in Fig. 2(a), is probed by a point source located at the origin of the coordinate system (see the green circle therein).

A measure of the dynamic response, directly accessible in vibrometric experiments, is the average mobility over a probing surface, that is, as follows:

$$\mathcal{M}(\omega) = \frac{\omega \langle |\psi(\mathbf{r}, \omega)| \rangle}{|F_0(\omega)|}, \quad (9)$$

where $F_0(\omega)$ is the time-Fourier transform of the input force on the plate, $\psi(\mathbf{r}, \omega)$ is the time-harmonic flexural field, $\langle \cdot \rangle = 1/S \int d^2\mathbf{r}(\cdot)$ is the average operator over a surface of area S , and $|\cdot|$ denotes the absolute value of a complex number. In computations, we assume $F_0(\omega) = 1$. The average mobility within a probing region [dashed rectangle in Fig. 2(a)] of the Penrose cluster is represented in Fig. 4(b) by the black solid curve, whereas the red line represents the average mobility of a honeycomb cluster region [dashed rectangle in Fig. 2(d)].

The two phononic crystals feature strong Bragg peaks, shown in Fig. 4(a). The black points refer to the Penrose lattice and are identical to those in Fig. 2(c), whereas the red dots are the smallest nonzero Bravais nodal points in reciprocal space associated with the triangular lattice.

The scattering of flexural waves within the Penrose cluster results in a plethora of local minima in mobility. We draw the reader's attention on a set of pronounced minima, marked by the associated frequencies (f_1 and f_2 for the Penrose cluster, and f^* for the honeycomb cluster). In addition, we observe that the mobility of the honeycomb cluster features attenuation consistent with the band gap associated with its periodic counterpart [see Fig. 8(a)] and marked by the red-shaded rectangle. Despite Eq. (7) is asymptotically equivalent to the “true” dispersion, only in the low-frequency long-wavelength regime, Fig. 3(b) shows that it provides a good estimation for the band-gap frequency. This suggests that Eq. (7) could be used to estimate an effective wave number of the mode within the cluster. Indeed, by substituting $\omega/(2\pi) = f^*$ into Eq. (7) we get $|\kappa| = 217.9 \text{ m}^{-1}$, very close to $|\mathbf{G}_1|$ reported in the caption of Fig. 4. A similar estimation starting from f_1 and f_2 , results in $|\kappa| = 143.4$ and $|\kappa| = 192.1 \text{ m}^{-1}$, respectively, within 5% from the reported values (see the caption of Fig. 4) for $|\mathbf{K}_1|$ and $|\mathbf{K}_2|$. This suggests that the attenuation regions featured by the Penrose cluster in Fig. 4(b) are indeed controlled by the Bragg peaks shown in Fig. 4(a). Moreover, such Bragg peaks are a clear fingerprint of the long-range order beyond periodicity. Indeed, the fact that special wave-vectors \mathbf{K}_1 and \mathbf{K}_2

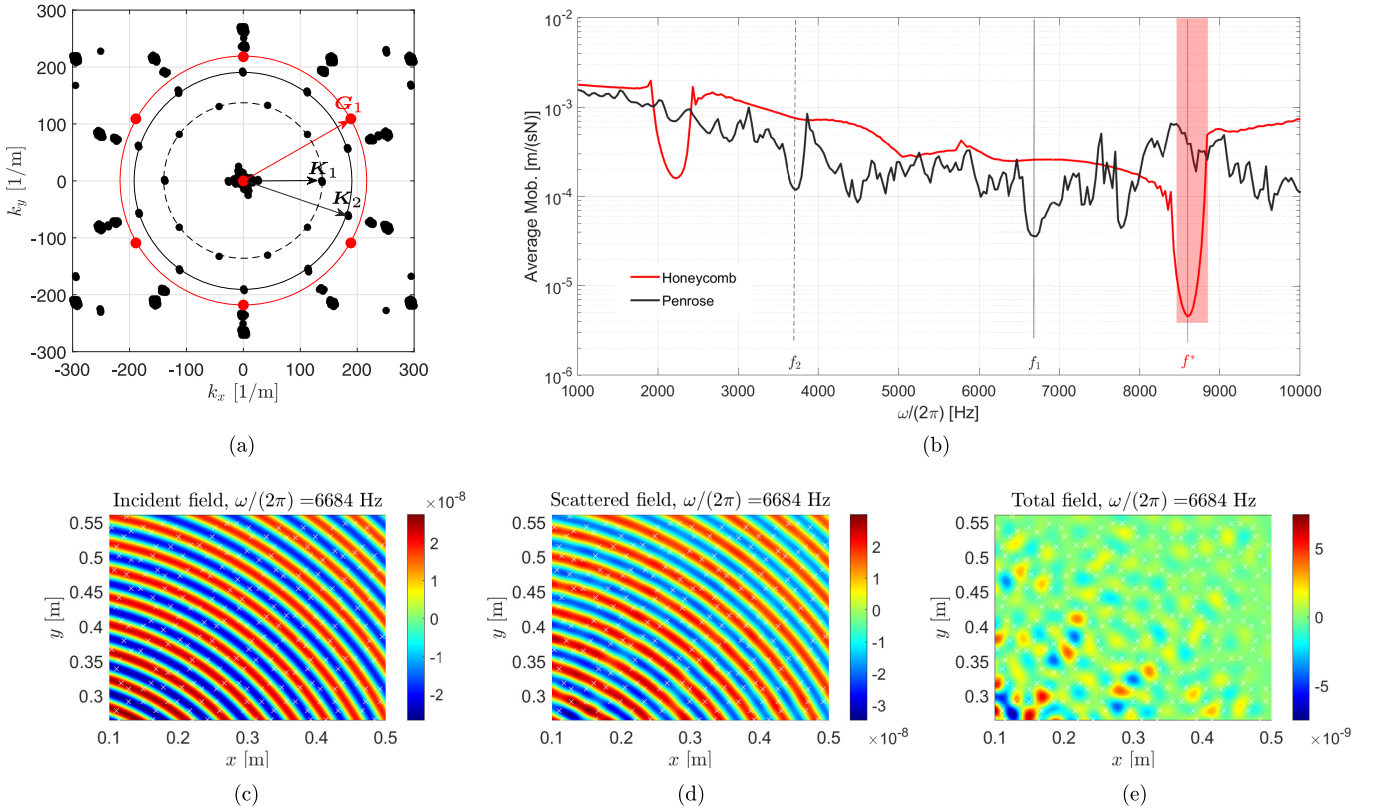


FIG. 4. Panel (a) shows the approximate Bragg peaks of the finite Penrose point-masses cluster (black dots) and the Bragg peaks of the honeycomb point-mass cluster (red lines) with equivalent density. The dashed and solid black circles with radii $|K_1| = 136.5 \text{ m}^{-1}$ and $|K_2| = 194.2 \text{ m}^{-1}$, respectively, comprise some of the tenfold symmetric Bragg peaks featured by the P3 Penrose lattice. The red circle with radius $|G_1| = 218.1 \text{ m}^{-1}$ comprise the sixfold symmetric Bragg peaks featured by the honeycomb lattice. Panel (b) shows the mobility of the finite clusters hosted by an infinite thin plate as a function of the frequency of the incident point source. Black and red lines refer to the Penrose and the honeycomb cluster, respectively. In panel (b), we also mark special frequencies at which local minima in mobility occur in both clusters ($f_1 = 3723.1 \text{ Hz}$ and $f_2 = 6684.2 \text{ Hz}$ for the Penrose cluster, and $f^* = 8600.3 \text{ Hz}$ for the honeycomb cluster). Panels (c)–(e) show the incident, scattered and total $[\psi(\mathbf{r})$ in Eq. (2)] flexural fields at $\omega/(2\pi) = f_2$ resulting from the multiple scattering method in Appendix A.

are lower in moduli than $|G_1| = |G_2|$ (the reciprocal lattice vector of the corresponding honeycomb lattice) suggests that they emerge from patterns whose length scale is larger than $\bar{\ell}$.

To further substantiate the previous claims, we illustrate the Bragg scattering nature of the attenuation in our P3 Penrose cluster by means of Figs. 4(c)–4(e). The panels show the incident, scattered, and total flexural fields, respectively, associated with the f_2 mobility minimum in Fig. 4(b). Figure 4(c) shows the incident flexural field emanating from the point source. Due to the fact that the point source is located close to the Penrose cluster, the probing region therein experiences an incoming flexural comprising a wide range of directions. The scattered field clearly shows similar wavefronts with the opposite phase compared to the incident field. The sum of the incident and scattered contributions (i.e., the total field) results in an overall attenuation of flexural waves. As Fig. 4 shows, the cancellation is not perfect, and clear localized modes emerge, away from the excitation point. Despite that, Fig. 4(e) demonstrates that the attenuation observed in the dynamic response is a coherent effect due to Bragg scattering.

C. Penrose studded plate mobility and localization

For a Penrose studded plate, a UC in the Bloch-Floquet sense does not exist. Nevertheless, insights can be gained by analyzing the dynamic response of a finite plate, subjected to a harmonic loading and to physical boundary conditions at the edges of the sample. The most straightforward way to model the aforementioned situation is by using the FE method. Specifically, we use a time-harmonic formulation with a unit forcing vector oriented normal to the plate. We repeat the computation for 450 equally spaced frequencies between 1 and 8 kHz, which being independent from one another can be readily parallelized for improved computational time efficiency. The rigid scatterers assumption for the studs is justified by an independent modal computation carried over a single elastic stud made out of brass and showing that its first nontrivial eigenmode is above 20 kHz, therefore, far away from our frequency range of interest. Appendix B [specifically, Fig. 8(b)] provides further arguments supporting the aforementioned modeling assumption. The contact between the rigid-body scatterer and the plate is of the bonded type, which assumes continuity of rotations and displacement at the plate/scatterers junctions.

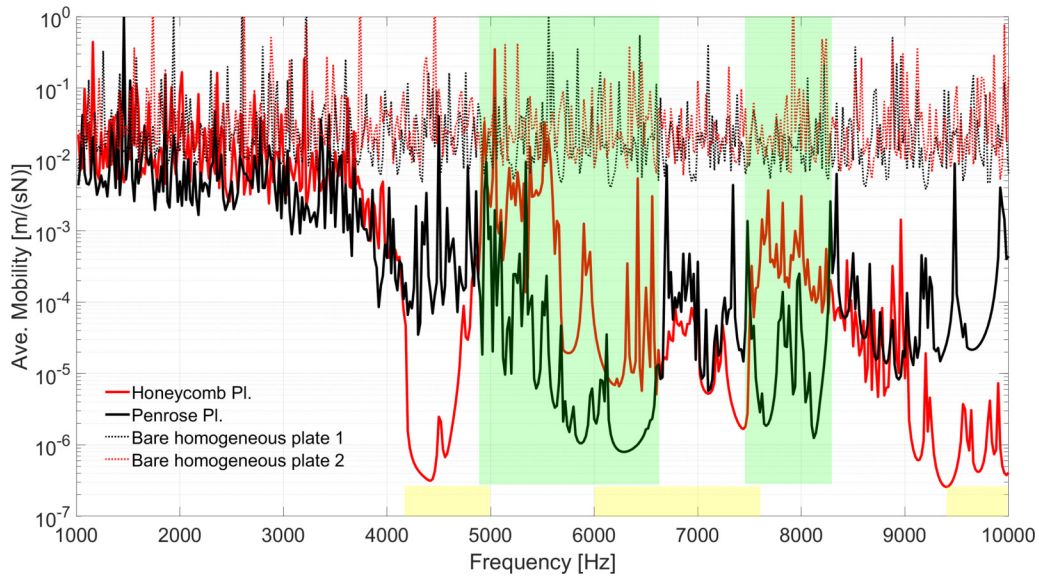


FIG. 5. Finite element (FE) average mobility of the two finite plates with traction-free boundary conditions. The black and red solid lines refer to the Penrose and honeycomb studded lattices, respectively. The material parameters used for both plates are reported in Table I. The red and black dotted lines represent the average mobility of homogenized plates (honeycomb and Penrose, respectively) with homogenous mass density as in Eq. (6). We mark band gaps (yellow-shaded rectangles) as predicted by Fig. 3(c). The green-shaded regions highlight frequency bands for which the flexural waves' attenuation in the Penrose plate outperforms that of the honeycomb counterpart.

In the same spirit as in Fig. 4, Fig. 5 compares the average mobility of the two finite plates subjected to a unit point force and complemented with traction-free boundary conditions at their boundaries. The black and red curves refer to the Penrose and honeycomb studded plates, respectively. Each stud is modeled as rigid as detailed in Appendix B. The yellow rectangles show the band gaps within the periodic plate as predicted in the context of Fig. 3(c). This is consistent with the low average mobility in those frequency ranges (see the red solid curve). As highlighted by the green-shaded areas in Fig. 5, the mobility of the Penrose plate is lower than the periodic counterpart in a wide range of frequencies.

In order to single out the effect of periodic and aperiodic orders, we report the average mobility of homogeneous finite plates (bare plate 1 and bare plate 2) with elastic parameters as in Table I and mass density as in Eq. (6). Such homogeneous counterparts only differ by the overall shape of the plate. We observe that, despite the bare plates differ by the overall shape, this affects only the fine modal behavior but not the mobility order of magnitude in such a broad frequency range. By direct comparison of the solid and dotted curves in Fig. 5, the studded plates result in strong attenuation compared to the homogeneous counterparts. Moreover, in the frequency regime from 3000 up to 9000 Hz, the realization of the Penrose plate analyzed in the current paper results in a consistently lower mobility. In turns, this results in the presence of Bragg peaks associated with aperiodic order. In order to test the predictive power of the numerical models, we have commissioned a plate with holes located at the blue dots in Fig. 2(a). We have, subsequently, screwed the studs described in Sec. III A into the holes, with sufficient torque to ensure bonded conditions. Figure 6 shows the setup of the vibrometric experiment. The Penrose plate is hung by the ceiling via two strings passing through two small holes. This configuration mimics traction

free boundary conditions, consistent with the numerical FE models. The resulting studded plate has been, subsequently, analyzed via laser Doppler vibrometry. Specifically, we drove a shaker (lower left corner of the plate in Fig. 6) using a frequency sweep (1–8 kHz). The resulting force between the stinger of the shaker and the plate, applied to the origin of the coordinate system in Fig. 2(a), is measured by interposing a force sensor. The resulting force signal is used as reference for the laser Doppler vibrometer—also marked in Fig. 6—thus, allowing a direct measurement of the mobility over a scanning region. The time-resolved data are collected and Fourier transformed in the time variable by the proprietary laser vibrometer software (Optomet). Spatially resolved experimental waveforms are, subsequently, exported and analyzed in Matlab.

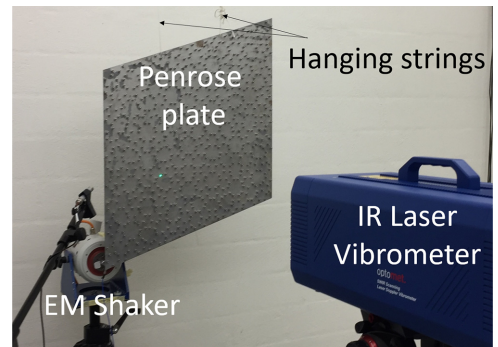


FIG. 6. Setup of the vibrometric experiment, whereby the Penrose studded plate, in nearly free boundary conditions, is excited by an electromagnetic shaker. The resulting flexural velocity field is measured via infrared laser Doppler vibrometry and the force between shaker and plate is used as reference for the calculation of the mobility.

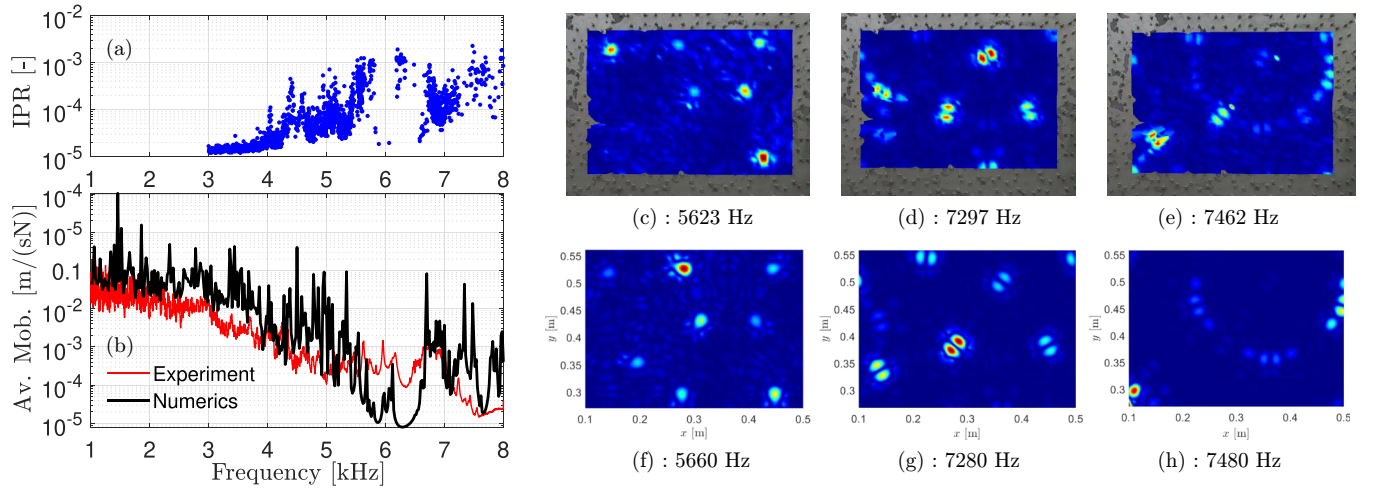


FIG. 7. Panel (a) shows the inverse participation ratio for the modal response of the Penrose plate see Eq. (10)]. Panel (b) compares the numerical average mobility (black solid line) and the average mobility obtained from vibrometric experiments (red solid line). Panels (c)–(e) show time-Fourier transform of the experimentally observed localized modes whereas panels (f)–(h) show the corresponding FE time-harmonic predictions.

Figure 7 compares our numerical predictions with the experimental observations, in similar regions of the Penrose studded plate (red and black solid curves, respectively).

In order to gain further insights on the effect of Bragg scattering within the Penrose plate, we have extracted the inverse participation ratio over the flexural components of the structural modes of the plates. By solving a modal analysis in ANSYS, and extracting the associated modes in the frequency range from 3000 to 8000 Hz, the inverse participation ratio (IPR) for the mode with frequency f_i is defined as [29]

$$\Pi(f_i) = \sum_{n=1}^N \Psi_n^4(f_i), \quad (10)$$

where Ψ_n , $n = \{1, \dots, N\}$ denote the nodal flexural mode of the plate and N denotes the total number of nodes. By assigning the mode normalization $\sum_{n=1}^N \Psi_n^2(f_i) = 1$, it is easy to realize that $\Pi(f_i)$ approaches 1 for very localized modes (i.e., only one node contributes 1, the remaining being zero), whereas $\Pi(f_i) \rightarrow 1/N$ for delocalized modes (each node equally contributes $1/\sqrt{N}$). In our numerical experiment, $N = 11\,085$ in the probing region.

The inverse participation ratio for the modal response of the Penrose studded plate is shown in Fig. 7(a). We highlight how the modal density of the plate is visibly low between 5500 and 6500 Hz. Moreover, as the frequency increases, several modes cluster towards high values of the IPR, suggesting a localized response within the plate. The IPR can be directly compared to the mobility curves shown in Fig. 6(b) (with red and black curve referring to experimental and numerical results, respectively).

The comparison between the experimental and the numerical mobility curves in Fig. 7(b) demonstrates a fair agreement of numerical and experimental results. More importantly, guided by Figs. 4(a) and 4(b), we are able to identify and experimentally observe localized mode shapes. The space-resolved experimental results [Figs. 7(c)–7(e)] and numerical [Figs. 7(f)–7(h)] waveforms indeed compare very well. Panels

(c) and (f) show highly localized waveforms far away from the source of vibration resulting in very attenuating response of the Penrose plate. In the latter, localized waveforms are observed only in the vicinity of the input location, in frequency regimes featuring quasizero group velocity and band gaps [30] or close to *ad hoc* defects in the periodicity [31]. In our P3 scatterers realization, localized modes emerge in the entire scanned region as shown in Figs. 7(b)–(d). The nature of such localized modes is reminiscent of “bound states in the continuum,” recently predicted in highly symmetric clusters of resonators hosted by homogenous plates [32]. According to the frequency of the input force, bare plate regions enclosed by rings of scatterers support monopole [see Figs. 7(c) and 7(f)] or dipole modes [see Figs. 7(d), 7(e), 7(g) and 7(h)]. Different from the predictions in Ref. [32], the localization in our P3 Penrose lattice does not result from the locally resonant nature of the scatterers but is rather due to Bragg scattering induced by the aperiodic order, similar to what we show in the context of Fig. 4(e).

IV. CONCLUSIONS

In conclusion, we have described analytically, numerically, and experimentally the dynamic response of a finite plate comprising scatterers arranged aperiodically according to a P3 Penrose tiling pattern (see Fig. 1). The comparison with an equivalent (i.e., featuring similar low-frequency dispersive properties) periodic counterpart shows that the Penrose lattice is able to attenuate vibrations in a wide frequency range, well below the Bragg frequency of a honeycomb equivalent lattice. In addition, the results singled out the effect of rotational inertia whose inclusion give rise to marked departures from the Bragg scattering of flexural wave only.

The long-range order in the P3 Penrose lattice results in strong Bragg wave vectors in reciprocal space, which, in turn, influences the dynamic response of the cluster. This is evident when a nonlocally resonant cluster is considered as in Fig. 4. The inclusion of rigid studs activate the rotational degree

of freedom (DOF) of the scatterers which is responsible for the departures from the simple picture of Bragg scattering dominated by purely vertical forces (point mass situation). Nevertheless, similar conclusions can be drawn even for the finite plate studded with rigid inclusions. Since Bragg-type attenuation in a P3 lattice happens at lower frequency compared to the equivalent periodic counterpart, the results are relevant for structural engineering applications where controlling the low-frequency response is critical. In addition, we have identified a wave localization frequency regime shaped by Bragg scattering within the aperiodic realization of the Penrose P3 tessellation. The control of such Bragg scattering induced localization in aperiodic plates may prove useful in the context of energy harvesting or to damp even further unwanted structural modes at desired frequencies.

ACKNOWLEDGMENTS

The present paper has been initiated under an Empa Internal Research Call scheme as Project No. 5213.00171.100.01. We gratefully acknowledge the funding that made this paper possible.

APPENDIX A: MULTIPLE-SCATTERING THEORY

Using the KKR [20,21] method, given an incident field ϕ_0 , which is the solution of the unperturbed problem, we can write the elastic field in an arbitrary position \mathbf{r} within the plate as

$$\psi(\mathbf{r}) = \phi_0(\mathbf{r}) + \int d^2\mathbf{r}_0 g_0(\mathbf{r}, \mathbf{r}_0; \beta) V(\mathbf{r}_0) \psi(\mathbf{r}_0), \quad (\text{A1})$$

where we have introduced the Green's function in Eq. (4), and $V(\mathbf{r}_0)$ is the right-hand side of Eq. (2). Specifically, the incident flexural displacement resulting from vertical load of amplitude F_0 at the origin of the coordinate system is

$$\phi_0(\mathbf{r}) = \frac{F_0}{D} g_0(\mathbf{r}, 0; \beta). \quad (\text{A2})$$

By using $V(\mathbf{r}_0) = \sum_{i=1}^{N_s} f(\beta) \delta(\mathbf{r}_0 - \mathbf{r}_i)$ in Eq. (A1), we obtain

$$\psi(\mathbf{r}) = \phi_0(\mathbf{r}) + f(\beta) \sum_{j=1}^{N_s} g_0(|\mathbf{r} - \mathbf{r}_j|) \psi(\mathbf{r}_j). \quad (\text{A3})$$

By taking the limit $\mathbf{r} \rightarrow \mathbf{r}_i$, the following linear system follows:

$$[\hat{1} - \hat{G}(\beta)]\psi = \phi, \quad (\text{A4})$$

where $[\hat{1}]_{ij} = \delta_{ij}$, $[\hat{G}(\beta)]_{ij} = t_j(\beta) g_0(|\mathbf{r}_i - \mathbf{r}_j|)$, $[\psi]_i = \psi(\mathbf{r}_i)$, $[\phi]_i = \phi(\mathbf{r}_i)$, and $i = 1, \dots, N_s$, from which ψ can be easily obtained, which completely determines the solution within the plate comprising scatterers and subjected to a point load.

APPENDIX B: EFFECT OF MODELING ASSUMPTIONS ON THE DISPERSIVE PROPERTIES OF THE PERIODIC COUNTERPARTS

In the present Appendix, we provide the details concerning two unit-cells model formulations, to calculate the dispersive properties of the honeycomb counterparts introduced in Sec. III. We address two practical modeling issues:

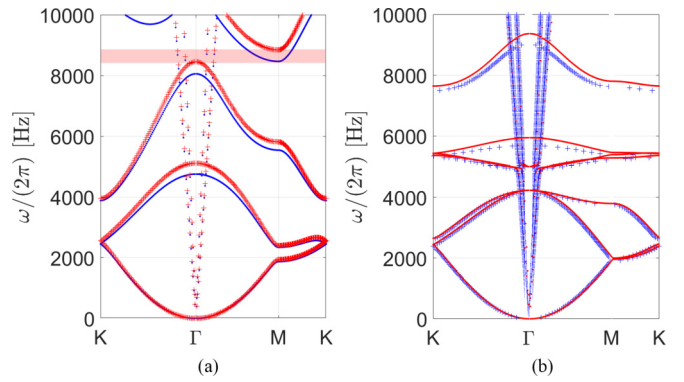


FIG. 8. Panel (a) compares the dispersion diagram in Fig. 3(b) (blue dots) to that of a homogeneous UC with concentrated mass over a small volume (red crosses). The Bragg band gap featured by the latter is also shown (red shaded area). Panel (b) compares the dispersion diagram in Fig. 3(c) (red points) to that of a shell model complemented with rigid scatterers (blue crosses) in Fig. 3(d).

the effect of the drilled holes, and the accuracy of using a “shell/rigid-scatterer” (S/RS) model compared to a full 3D model. Figure 8 illustrates both questions.

1. Bloch-Floquet analysis

The 3D displacement \mathbf{u} of a solid within linear, isotropic, time-harmonic elastodynamics is governed by the Navier-Cauchy equation,

$$\mu \nabla^2 \mathbf{u} + (\lambda + \mu) \nabla(\nabla \cdot \mathbf{u}) - \rho \omega^2 \mathbf{u} = 0, \quad (\text{B1})$$

with μ and λ being the Lamé parameters, i.e., $\mu = E/[2(1 + \nu)]$ and

$\lambda = E\nu/[(1 + \nu)(1 - 2\nu)]$. Equation (B1) holds within domains with different material properties, such as the plate and studs for UC2 in Fig. 3(a). Within standard commercial FE solvers, compatibility among the displacement in multimaterial regions can be imposed by requiring perfectly bonded contact, i.e., continuity of displacement and normal tractions in the junction area. Doubly periodic media support special solutions to Eq. (B1) of the form

$$\mathbf{u}(\mathbf{r} + \mathbf{t}, z) = e^{i\mathbf{\kappa} \cdot \mathbf{t}} \mathbf{u}(\mathbf{r}, z), \quad (\text{B2})$$

where $\mathbf{\kappa}$ is the two-dimensional Bloch-Floquet wave number, z is the out-of-plane coordinate, and \mathbf{t} is any integer linear combination of the lattice vectors. After FE discretization, e.g., using COMSOL MULTIPHYSICS, Eq. (B1) complemented with Bloch-Floquet boundary conditions (B2), results in a linear algebraic eigenvalue problem for the Bloch frequency ω , as a function of the Bloch-vector $\mathbf{\kappa}$ within the first Brillouin zone (the so-called *indirect method*). Bloch-Floquet analysis in periodic FE-discretized structures can be also performed using the so-called *direct method* where a polynomial eigenvalue problem is solved for the complex Bloch wave vectors as a function of frequency. For further details, the reader is referred to Refs. [33,34].

2. Model formulations

In Fig. 8(a), we compare the dispersion diagram in Fig. 3(a) (here represented by the blue crosses) with that of a 3D solid model *without holes* where the scatter mass is concentrated into a cylinder of the same height as the plate and radius $r = 1$ mm (see the red dots). For both computations, the direct method is used. The comparison shows that the presence of the holes shifts frequencies slightly upwards but does not qualitatively alter the dispersion diagrams. In what follows, we opt to retain the holes.

An alternative natural FE framework to accommodate the rotational inertia of the scatterers compared to 3D elasticity is provided by shell models [Reissner-Mindlin plate theory [35]] are encoded into the SHELL281 element [36]. The formulation differs from Kirchhoff's theory in Eq. (3) due to the account of first-order shear deformation effects and rotational inertia of the plate, which in the present paper are kept small by design, the minimum wavelength being $\lambda_{\min} > h/6$. Nevertheless, in finite element routines, the kinematics of plates account for displacement the rotation fields as independent variables, allowing to consistently define boundary conditions of the plate's rotational and translational degrees of freedom with the rotations and translations of the rigid studs. The rigid bodies associated with each scatterer feature 6 DOFs, whose compatibility with the shell rotations and translations is prescribed within the software. This allows to numerically build a reduced order model with

significantly less degrees of freedom compared to that resulting from the solid element formulation as each finely resolved 3D scatterer is reduced to 6 degrees of freedom only.

Figure 8(b) compares the dispersion diagram in Fig. 3(b) (stemming from 3D elastodynamics, here represented by the red dots) with that of a S/RS model where the shell is discretized with quadratic elements (10 344 DOFs in total). The discretization mesh of the elastodynamics unit-cell (UC2) is shown in Fig. 3(a) and features 463 224 DOFs. Despite the different formulations, direct inspection of Fig. 8(b) shows that the S/RS model captures very well the dispersive properties of the studded phononic crystal. This encourages us to use a similar reduced formulation for the Penrose plate (see Sec. III C). A mesh convergence study has shown that the spatial discretization proposed here is adequate (error of less than 1%) in predicting eigenfrequencies with traction-free boundary conditions up to ≈ 11 kHz.

The dispersion diagram associated with the reduced shell UC is solved using the direct method within the wave-finite element (WFE) formulation [34] and with the help of the Matlab "polyeig" function. In Ref. [33], we have shown that the WFE solution space can be efficiently restricted to the IBZ border. This is precisely what we show in Fig. 8(b) by means of the blue crosses whereby only the purely real solutions have been included to facilitate the comparison with the indirect method calculation (red points).

-
- [1] D. Shechtman, I. Blech, D. Gratias, and J. W. Cahn, Metallic Phase with Long-Range Orientational Order and No Translational Symmetry, *Phys. Rev. Lett.* **53**, 1951 (1984).
 - [2] R. McPhedran, A. Movchan, and N. Movchan, Platonic crystals: Bloch bands, neutrality and defects, *Mech. Mater.* **41**, 356 (2009).
 - [3] A. Movchan, N. Movchan, and R. McPhedran, Bloch–floquet bending waves in perforated thin plates, *Proc. R. Soc. A* **463**, 2505 (2007).
 - [4] M. Farhat, S. Guenneau, S. Enoch, A. B. Movchan, and G. G. Petursson, Focussing bending waves via negative refraction in perforated thin plates, *Appl. Phys. Lett.* **96**, 081909 (2010).
 - [5] N. Movchan, R. McPhedran, A. Movchan, and C. Poulton, Wave scattering by platonic grating stacks, *Proc. R. Soc. A* **465**, 3383 (2009).
 - [6] S. Haslinger, N. Movchan, A. Movchan, and R. McPhedran, Transmission, trapping and filtering of waves in periodically constrained elastic plates, *Proc. R. Soc. A* **468**, 76 (2012).
 - [7] C. Poulton, A. Movchan, N. Movchan, and R. C. McPhedran, Analytic theory of defects in periodically structured elastic plates, *Proc. R. Soc. A* **468**, 1196 (2012).
 - [8] T.-T. Wu, Z.-G. Huang, T.-C. Tsai, and T.-C. Wu, Evidence of complete band gap and resonances in a plate with periodic stubbed surface, *Appl. Phys. Lett.* **93**, 111902 (2008).
 - [9] D. Torrent, D. Mayou, and J. Sánchez-Dehesa, Elastic analog of graphene: Dirac cones and edge states for flexural waves in thin plates, *Phys. Rev. B* **87**, 115143 (2013).
 - [10] M. Gei, Z. Chen, F. Bosi, and L. Morini, Phononic canonical quasicrystalline waveguides, *Appl. Phys. Lett.* **116**, 241903 (2020).
 - [11] B. Van Damme, L. Matar, G. Hannema, D. Tallarico, A. Zemp, and A. Bergamini, Bending-wave localization and interaction band gaps in quasiperiodic beams, *Phys. Rev. B* **103**, 094301 (2021).
 - [12] M. I. Rosa, Y. Guo, and M. Ruzzene, Exploring topology of 1d quasiperiodic metastructures through modulated lego resonators, *Appl. Phys. Lett.* **118**, 131901 (2021).
 - [13] D. Beli, M. I. N. Rosa, C. De Marqui, Jr., and M. Ruzzene, Mechanics and dynamics of two-dimensional quasicrystalline composites, *Extreme Mech. Lett.* **44**, 101220 (2021).
 - [14] D. Beli, M. I. N. Rosa, C. D. Marqui, Jr., and M. Ruzzene, Wave beaming and diffraction in quasicrystalline elastic metamaterial plates, *Phys. Rev. Res.* **4**, 043030 (2022).
 - [15] R. Penrose, A class of non-periodic tilings of the plane, *Math. Intelligencer* **2**, 32 (1979).
 - [16] U. Grimm, Highly symmetric aperiodic structures, *EPJ Web Conf.* **255**, 09001 (2021).
 - [17] S. Eddins, Penrose rhombus tiling (<https://github.com/mathworks/penrose-tiling>).
 - [18] J. E. S. Socolar and P. J. Steinhardt, Quasicrystals. ii. unit-cell configurations, *Phys. Rev. B* **34**, 617 (1986).
 - [19] K. Watanabe, *Integral Transform Techniques for Green's Function* (Springer Cham, Berlin, 2014).
 - [20] J. Korringa, On the calculation of the energy of a bloch wave in a metal, *Physica* **13**, 392 (1947).
 - [21] W. Kohn and N. Rostoker, Solution of the schrödinger equation in periodic lattices with an application to metallic lithium, *Phys. Rev.* **94**, 1111 (1954).

- [22] L. L. Foldy, The multiple scattering of waves. i. general theory of isotropic scattering by randomly distributed scatterers, *Phys. Rev.* **67**, 107 (1945).
- [23] G. Carta, D. Colquitt, A. Movchan, N. Movchan, and I. Jones, Chiral flexural waves in structured plates: directional localisation and control, *J. Mech. Phys. Solids* **137**, 103866 (2020).
- [24] R. Wiltshaw, J. M. De Ponti, and R. V. Craster, Analytical solutions for bloch waves in resonant phononic crystals: Deep subwavelength energy splitting and mode steering between topologically protected interfacial and edge states, *Q. J. Mech. Appl. Math.* **2023**, hbad001 (2023).
- [25] Eq. 1 can be recast into the matrix form $\mathbf{N}^{(n)} = \hat{M}^{n-1} \mathbf{N}^{(1)}$ with
- $$\hat{M} = \begin{pmatrix} 1 & 1 \\ 1 & 2 \end{pmatrix}. \quad (\text{B3})$$
- [26] D. Tallarico, N. V. Movchan, A. B. Movchan, and D. J. Colquitt, Tilted resonators in a triangular elastic lattice: Chirality, bloch waves and negative refraction, *J. Mech. Phys. Solids* **103**, 236 (2017).
- [27] M. Baake and U. Grimm, *Aperiodic Order: A Mathematical Invitation*, Aperiodic Order (Cambridge University Press, Cambridge, UK, 2013), Vol. 1.
- [28] Customer information sheet, <https://docs.rs-online.com/5260/0900766b8136e812.pdf>, accessed: 2022-06-27.
- [29] C. E. Máximo, N. Piovella, P. W. Courteille, R. Kaiser, and R. Bachelard, Spatial and temporal localization of light in two dimensions, *Phys. Rev. A* **92**, 062702 (2015).
- [30] D. Tallarico, A. Trevisan, N. V. Movchan, and A. B. Movchan, Edge waves and localization in lattices containing tilted resonators, *Front. Mater.* **4**, 16 (2017).
- [31] F. Li, J. Liu, and Y. Wu, The investigation of point defect modes of phononic crystal for high q resonance, *J. Appl. Phys.* **109**, 124907 (2011).
- [32] M. Martí-Sabaté, B. Djafari-Rouhani, and D. Torrent, Bound states in the continuum in circular clusters of scatterers, *Phys. Rev. Res.* **5**, 013131 (2023).
- [33] D. Tallarico, G. Hannema, M. Miniaci, A. Bergamini, A. Zemp, and B. Van Damme, Superelement modelling of elastic metamaterials: Complex dispersive properties of three-dimensional structured beams and plates, *J. Sound Vib.* **484**, 115499 (2020).
- [34] B. R. Mace and E. Manconi, Modelling wave propagation in two-dimensional structures using finite element analysis, *J. Sound Vib.* **318**, 884 (2008).
- [35] I. Elishakoff, F. Hache, and N. Challamel, Vibrations of asymptotically and variationally based uflyand–mindlin plate models, *Int. J. Eng. Sci.* **116**, 58 (2017).
- [36] ANSYS Element Reference, Release 2022 R2, 2022